Pattern formation during laser melting of silicon

J. S. Preston,* H. M. van Driel, and J. E. Sipe

Department of Physics and Erindale College, University of Toronto, Toronto, Ontario, Canada M5S 1A7

(Received 11 July 1988)

Silicon films under intense, continuous laser irradiation at $\lambda = 10.6$ μm develop into spatially inhomogeneous molten states. The systematic study of the different patterns as a function of laser intensity and spot size reveals a variety of ordered and disordered states. For small spot size, highly correlated, long-range periodic structures (gratings) with spatial periods of $\lambda, 2\lambda, 3\lambda, \ldots$ are observed for increasing intensity. For low intensities and large spot sizes, irregular molten and solid lamellae are observed with only short-range order. We show that the ordered and disordered molten structures reflect different levels of balance between spatially coherent energy deposition from the laser and heat flow from the illuminated region. Changes in the intensity or spot size can be used to alter the balance and induce morphological "phase transitions" between the different structures. We find that many of the characteristics of the patterns, including the spacings of the periodic structures and the size and separation of the lamellae, can be explained by the theory of the electrodynamic response of optically inhomogeneous surfaces presented in the preceding paper.

I. INTRODUCTION

Coherent light has been used to process materials since the development of the first laser.[1] In these applications lasers are chosen over other energy sources because of the localized, high power densities they offer. The small spot size associated with laser radiation is, of course, directly related to the coherence properties of the beam. This coherence is, however, the source of various types of instabilities in laser-material processing. One of the best known of these is related to the interference between an incident beam and a surface scattered field.[2-8] Here the breaking of the translational symmetry of the surface by roughness leads to inhomogeneous and often periodic melting, etching, and photodeposition at high laser intensities. For picosecond and nanosecond laser pulses it has been shown that the instability is almost entirely electrodynamic in origin, with the spacings and orientations of the structures related to the properties of the beam and of the material. This is not entirely unexpected, since on these short-time scales thermodynamic or mechanical forces associated with heat flow or material viscosity are unimportant over distances of the order of the wavelength or the absorption depth, which are typically microns.

The first observations of patterns under continuous-wave (cw) laser melting were reported by Bosch and Lemons in 1981.[9] It was noted that laterally segregated molten and solid regions develop during melting of silicon films by a 0.5 μm laser. Later, studies by Biegelsen and co-workers using a 10.6 μm laser revealed the existence of an ordered melt pattern consisting of alternate molten and solid strips with a periodicity equal to the incident wavelength.[10] An intuitive argument[11] can be made against the existence of a uniform phase, based upon the different reflectivities of solid and molten silicon. Molten bulk silicon is metallic and has a much higher reflectivity ($\simeq 0.9$) than that ($\simeq 0.3$) of the semi-

conducting solid phase. This leads to a range of laser intensities near the melting threshold for which a uniform solid surface would absorb too much energy and try to melt, while a uniform molten surface would reflect too much light and try to solidify. Since neither uniform phase is possible, a spatially inhomogeneous state, with an average reflectivity between that of the solid and liquid, must result.

In this paper we show that the melt patterns that are observed on silicon under cw radiation result from the same electrodynamic processes as the ripple patterns that occur during pulse laser melting. The pulsed laser patterns that form on solids are, to a large extent, determined by the inhomogeneous energy deposition that occurs prior to melting. But, as we shall show, the patterns that form for continuous illumination self-consistently result from a balance between the light absorption of the composite melt-solid inhomogeneous phase and the heat flow out of the illuminated region. Therefore, in the cw case both electrodynamics and thermodynamics play a role. In an earlier brief report[12] of the results presented here we showed that the interplay between the deposition of coherent energy in a composite dielectric-metallic structure and the heat flow results in a loss of many of the universal[13] properties that characterize pulsed-laser-induced structures. The spectrum of spacings and orientations of structures occurring in the pulsed case is replaced by a new, diverse set of steady-state structures many of which do not occur in the pulsed case and which have also not been observed by others in the cw case. Many of these patterns are stable against substantial variations of the laser intensity and can therefore be identified as morphological phases[12] of a system driven far from equilibrium. One can identify the laser-induced morphologies as a particular example of the class of pattern-formation processes that occur in various nonequilibrium physical, chemical and biological systems.[14] In our experiments the pattern formation results

because of the synergy between absorption and heat flow via a material response. Details concerning the connection between the structures observed here and the broader class of pattern formation in nonequilibrium systems will not be addressed here but will be the subject of a future publication. In this paper we will concentrate on the description of the patterns and the understanding of these patterns from an electrodynamics and thermodynamics viewpoint.

The remainder of this paper is organized as follows. In Sec. II we discuss the samples and experimental techniques used to perform the studies. Section III summarizes the observations in which we illustrate the spectrum of patterns produced under different conditions when thin films of silicon are illuminated by 10.6-μm laser radiation. In Secs. IV and V we employ the theory of the previous paper[15] to show how electrodynamic considerations can self-consistently explain the various ordered and disordered patterns, respectively. Section VI summarizes our findings.

II. EXPERIMENTAL DETAILS

The experimental arrangement used to produce and study the melt structures in silicon thin films is shown in Fig. 1. A linearly polarized TEM_{00} beam from a continuous 20-W, 10.6-μm CO_2 laser was focused onto silicon on sapphire samples at normal incidence. Intensity fluctua-
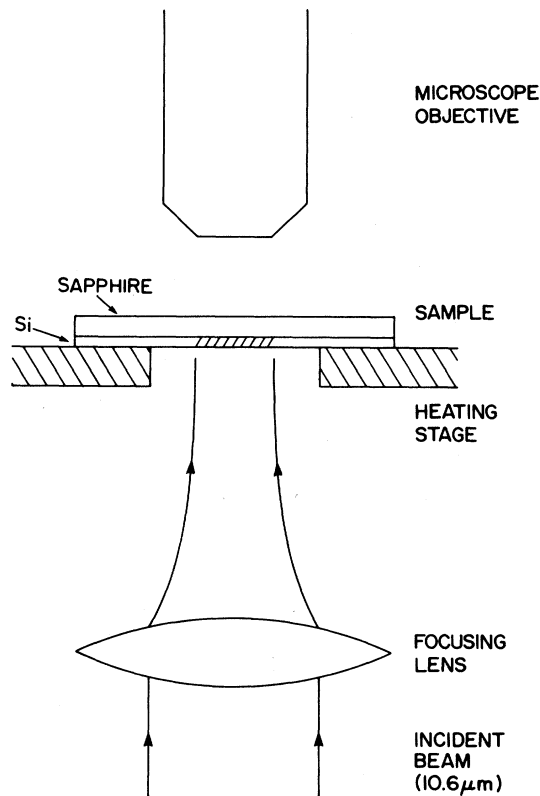

FIG. 1. Schematic diagram of method to produce and observe inhomogeneous melt structures on silicon.

tions of the laser could be kept below 2%. The spot size (FWHM of intensity) was typically a few hundred microns in diameter and could be controlled by positioning a 10-cm focal length lens. The samples were oriented with the film side facing the incoming laser beam. They were supported near the edges by a heating stage with the laser beam having access to the central portion of the film. The metal patterns produced in the silicon film were observed by spatially resolving the visible black-body emission through the transparent sapphire substrate. Although the temperature of the solid and molten portions of the film were not significantly different, the difference in their emissivities enabled the observation of the melt patterns. The patterns were observed through an optical (visible-light) microscope with a 10$\times$ objective and could be recorded with either a still or video camera attachment. Spacings in the observed patterns and other geometrical features were determined after performing appropriate calibration procedures.

The results reported here were all obtained with samples which were cleaved from the same wafer of a 2-μm-thick vapor-deposited (polycrystalline) silicon film on a 1-mm-thick sapphire substrate. Experiments performed with 0.5-μm-thick films gave essentially the same results indicating that for such thin samples the film thickness does not influence the pattern selection. However, the sample dimensions and shape were found to influence details (but not the qualitative features) of pattern development because of alterations in heat-loss efficiency. (The term "heat-loss efficiency" refers here to the rate of energy removal from the central portion of the irradiated area relative to its average temperature. When so defined it is closely associated with the melt threshold of the sample.) To minimize these geometry-related effects the sample size and shape were standardized; all were square pieces of width 2.5$\pm$0.1 mm. The optical and thermal properties of the samples are indicated in Table I.

A resistive heating stage was used to assist the laser in bringing samples to the melting point. The absorption

TABLE I. Material and optical properties [values taken from *American Institute of Physics Handbook* (AIP, New York, 1985) and E. H. Wolf, *Silicon Semiconductor Data* (Pergamon, Toronto, 1969)] of silicon and sapphire (MKS units).

Property	Silicon	Sapphire
Melting point	1680 K	2053 K
Thermal conductivity (solid)	22	29
Thermal conductivity (liquid)	67	
Heat capacity (solid)	700	810
Dielectric constant[a]	9.5+2i	0.45+0.1i
Reflectivity (λ=10.6 μm, $T \simeq$ 1680 K)	0.3	0.04
Dielectric constant	$-30+800i$	
Reflectivity (λ=10.6 μm, $T >$ 1680 K)	0.9	0.04

[a]Estimate based on ϵ(300 K)=11.8 and a thermally excited electron-hole carrier density of 10^{19} cm^{-3} at the melting point.

coefficient of silicon at 10.6 μm is governed by free carrier-absorption effects. Because the carrier density of an intrinsic semiconductor varies faster than exponentially with temperature, the absorption coefficient does as well and for silicon varies from less than 1 cm^{-1} at room temperature to 4×10^3 cm^{-1} at the melting point. For a sample initially at room temperature the direct heating of silicon by a continuous beam is therefore difficult to control because of runaway effects in sample temperature. To overcome this the samples were mounted on a pair of silicon strips (3 mm$\times$0.5 mm$\times$4 cm) which were resistively heated by dc currents as large as 5 A. A thin ceramic washer was positioned between the strips and samples to minimize lateral heat flow. The heater could bring the samples to approximately 800 K which was found to be a suitable starting temperature from which to control the sample by laser heating. At the melting point more than 60% of the unreflected laser power is deposited in the thin film with the remainder absorbed through the bulk of the sapphire substrate.

III. SPECTRUM OF PATTERNS: OBSERVATIONS

When samples were mounted as indicated above, two parameters were empirically found to determine the pattern selection. These were the intensity of the incident laser beam and the heat loss efficiency from the irradiated region. The heat-loss efficiency can be controlled by changing the laser spot size since the rate of energy removal scales with the perimeter of the irradiated region, whereas the total energy deposited will be proportional to the area. For a given average temperature, therefore, the thermal conduction per unit area will be greater for a smaller spot size.

Figures 2 and 4 show some of the different morphologies that could be created for different laser intensities or spot sizes. The series of photographs contained in Fig. 2 show, for increasing intensity, the progression of ordered morphologies which are created for small spot sizes ($\simeq 500$ μm). As the intensity increases above the melting threshold an ordered grating pattern develops, as Fig. 2(a) shows, with spacing equal to 10.5 ± 0.1 μm and with the wave vector of the grating parallel to the polarization of the beam. The fraction of the surface that is molten is approximately 50%. Note that although the laser intensity varies across the spot, the grating morphology is uniform up to the boundary. With the spot size constant, when the laser intensity is increased by as much as 30% beyond the threshold for grating formation the visual appearance of the grating does not change. Beyond this range the center of the spot forms a grating with a period of 21 ± 0.2 μm, as Fig. 2(b) shows. This structure corresponds to $\simeq 75\%$ of the center spot being molten, and this new morphology remains stable for increases of intensity by as much as 10%. To distinguish between these two grating patterns in this article, the first grating will be referred to as a simple grating, while the second grating will be referred to as a doubled grating. At intensities just below the threshold for complete melting, tripled (spacing 31 ± 1 μm) and quadrupled (spacing 40 ± 2 μm) gratings could form. However, these are generally not

the final steady states, and they evolve into different types of ordered two-dimensional arrays of isolated solid regions such as the one shown in Fig. 2(c). The exact nature of the array was difficult to control or even anticipate and seemed to be very sensitive to the experimental conditions including the history of the sample to the time of formation.

Figure 3 summarizes how the fraction of melt varies with local intensity for the ordered structures. The solid curve, which is deduced from observations of more than ten samples, is conservatively estimated to be accurate to $\pm5\%$. Nonetheless it indicates the existence of well-defined plateau regions and the formation of morphological phases which are stable against intensity fluctuations.

For large spot sizes (> 650 μm) no ordered structures were produced between the threshold of melting and the uniform melt phase. At the lowest intensity, as shown in Fig. 4(a), one has isolated molten discs of near elliptical shape separated from each other by an average distance of $\simeq 15$ μm. With increasing intensity the discs would coalesce to form disordered lamellae strings of increasing lateral extent and then continuously evolve into what would be viewed as solid-string lamellae in a molten background, as Fig. 4(b) indicates. While this pattern lacks long-range order it clearly is not random, with the separation between adjacent molten regions being well defined. At high intensities, the topology of the melt pattern reverses as the melt pattern displays isolated solid regions within a molten silicon background. This topological change occurs at $f_m \simeq 0.5$. Just before the onset of uniform melting the center of the spot would contain isolated solid discs as indicated in Fig. 4(c). In the central portion of the laser spot the solid regions appeared to drift independently except for occasional "collisions." By this we mean that the temperature fields change so that some material melts and other material solidifies, causing the outline of the solid region to translate: There is essentially no material actually moving in the thin film. For large spot sizes the transition from the uniform solid to the uniform molten stage occurred in less of a steplike fashion than for the smaller spot sizes as Fig. 3(b) of Ref. 13 shows. Even in this case, however, the fraction of melt does not increase linearly with intensity.

A summary of the types of patterns that form for different laser intensities and spot sizes can be presented in the form of a nonequilibrium stability diagram, analogous to the phase diagram of an equilibrium system. This is shown in Fig. 5. Regions I and VIII correspond to the silicon film being completely solid or molten, respectively. The rest of the diagram represents the various patterns the partially molten silicon film forms in steady state. The identification of distinct structures was based on properties of the melt pattern such as its symmetry and the percentage of the surface that was molten. The axes of the diagram are the intensity and the inverse diameter of the incident laser beam. One obvious trend in the figure is that a decrease in the spot diameter leads to an increase in the heat-loss efficiency, and as a result, a higher melting threshold. The spot diameter also has a role in the pattern formation process within the melt-solid coexistence region. The melt structures represent-
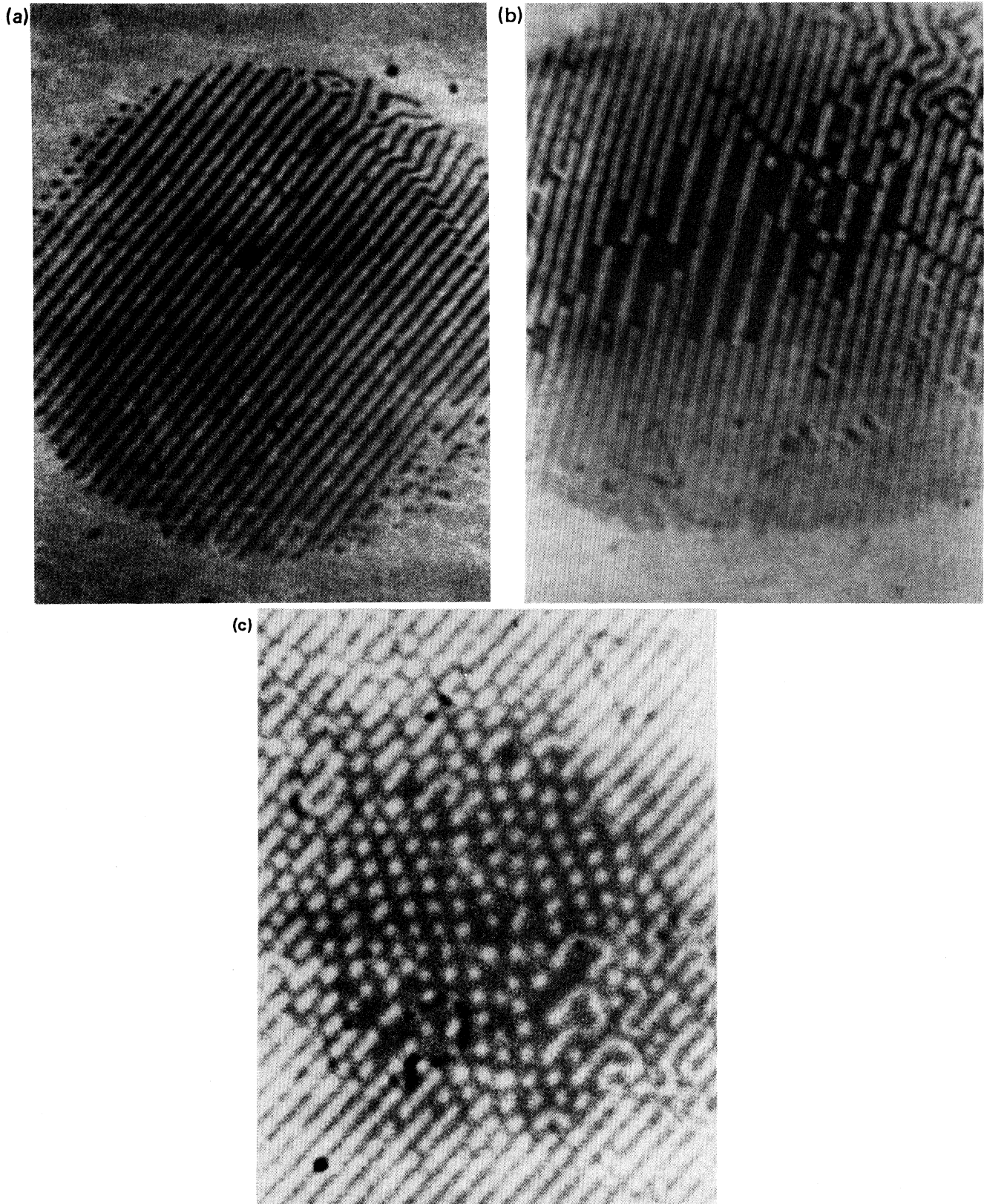
FIG. 2. Photographs of laser-generated melt patterns which exhibit long-range order for a spot size of 500 μm: (a) that of a simple grating of period 10.5±0.1 μm occurring for a laser intensity of 2.7 kW cm^{-2} corresponding to region III in Fig. 5; (b) photograph of the interior portion of a spot illuminated at 3.2 kW cm^{-2}; the simple grating has been replaced by the doubled grating structure; (c) in the central portion of the photograph, the solid regions are aligned in the lamellae array pattern. The laser intensity is 3.4 kW cm^{-2}.

ed on the right side of the diagram display long-range order while disordered melt structures are associated with regions II, VI, and VII. Small spot sizes, and hence large heat-loss efficiencies, lead to melt structures being formed with long-range order. The ordering of melt structures resulting from small spot diameters could be a simple manifestation of the higher intensities required to initiate melting. At higher intensities the redistribution of coherent light should be more effective at forcing the system into an ordered state. The timescale associated with the formation of the melt patterns is much larger for the disordered patterns so that it is possible that the disordered states are not steady states at all, but rather metastable states of the system analogous to glasslike states of solids.

The precision of the measurements of both the intensity and diameter of the laser beam depended somewhat on the corresponding location in the stability diagram; however, both were typically measured to within $\simeq 5\%$. Small variations in the sample size and the details of the thermal coupling between the sample and the environment led to variations in the positions of the boundaries between different regions of up to 5% between different samples. Thus, while the stability diagram in Fig. 2 depicts the correct relationships between the nonequilibrium states of a particular silicon film under laser radiation, it can only provide crude quantitative information about quantities which were sample specific, such as the absolute value of the initial melting threshold, and the slopes of the transition line.

The melt patterns displayed hysteresis both with respect to changes in spot size and laser intensity. This could occur for two reasons. Difficulties associated with the initial nucleation of molten regions resulted in a
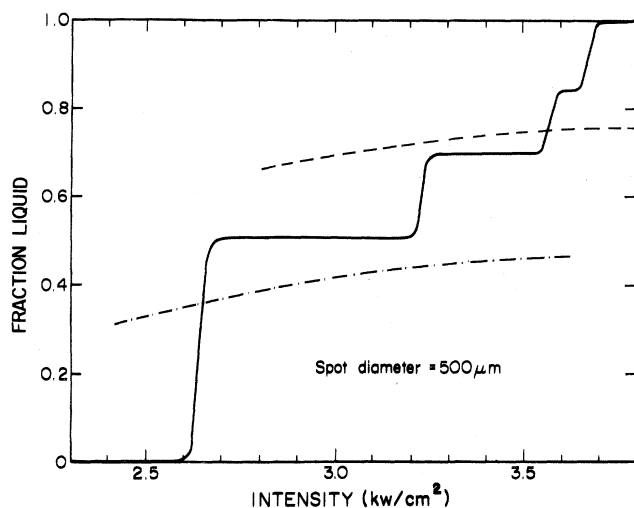
steady-state pattern formation time as long as several minutes in region II, if the film was previously completely solidified. However, if the film's state was brought into region II from a higher intensity state, the melt pattern relaxed to a steady state in a few seconds, and the position of the boundary between regions I and II was determined by lowering the intensity. In the other regions of the stability diagram, steady state was reached in time less than 3 sec. The second source of hysteresis arose at the boundaries between the ordered and disordered portions of Fig. 5. It was observed that perturbing a disordered pattern could lead to an irreversible transition to the corresponding ordered melt pattern. This behavior was observed only near the boundaries which separate disordered and ordered structures; at large spot diameters it was not possible to drive the melt pattern into an ordered state. The location of the boundaries was taken to be at the largest spot diameter for which the structure could be driven into an ordered state. In this case the hysteresis can probably be associated with frustration preventing the motion of the solid regions of the disordered structures. Further evidence is provided by the observation that "defects" in an ordered structure can only be removed by the defects migrating to the edge of the irradiated region.

The ceramic washer was found to be important in ensuring radially symmetric heat loss from the illuminated region. In an early phase of the work, with the sample mounted directly on the heater strip, heat flow to the strip occurred in a preferred direction. This broke the intrinsic symmetry of the sample, with the result that the direction of heat loss could influence the orientation of some of the structures. With the circular ceramic washer the experimental geometry enables the role of the incident light in the pattern formation process to be observed without being complicated by competition with lateral heat flow. Lateral heat loss can be considered a finite size effect, which vanishes in the case of the "ideal" experiment, plane wave incident upon a sample of infinite lateral extent.

IV. DISCUSSION

The gratinglike structure, shown in Fig. 2(a), is the simplest of the ordered melt patterns observed. The intimate connection between the grating pattern and the properties of the incident light are displayed both through the orientation and spacing of the grating. Experiments in which the polarization was varied, leaving other experimental parameters such as crystal orientation unchanged, indicated that the orientation of the pattern was determined by the polarization of the light. The fact that the periodicity of the simple grating is apparently equal to the wavelength of the incident light is indicative of the importance of the scattered electromagnetic field in producing the melt structure. According to the grating formula, light normally incident on a grating with a spacing Λ will be diffracted in directions, described by θ_n, that satisfy $\sin\theta_n = n\lambda/\Lambda$, where λ is the incident wavelength and n is an integer. If $\Lambda = \lambda$, the first-order diffracted beam is predicted to propagate along the surface. It is not possible to obtain a solution to Maxwell's
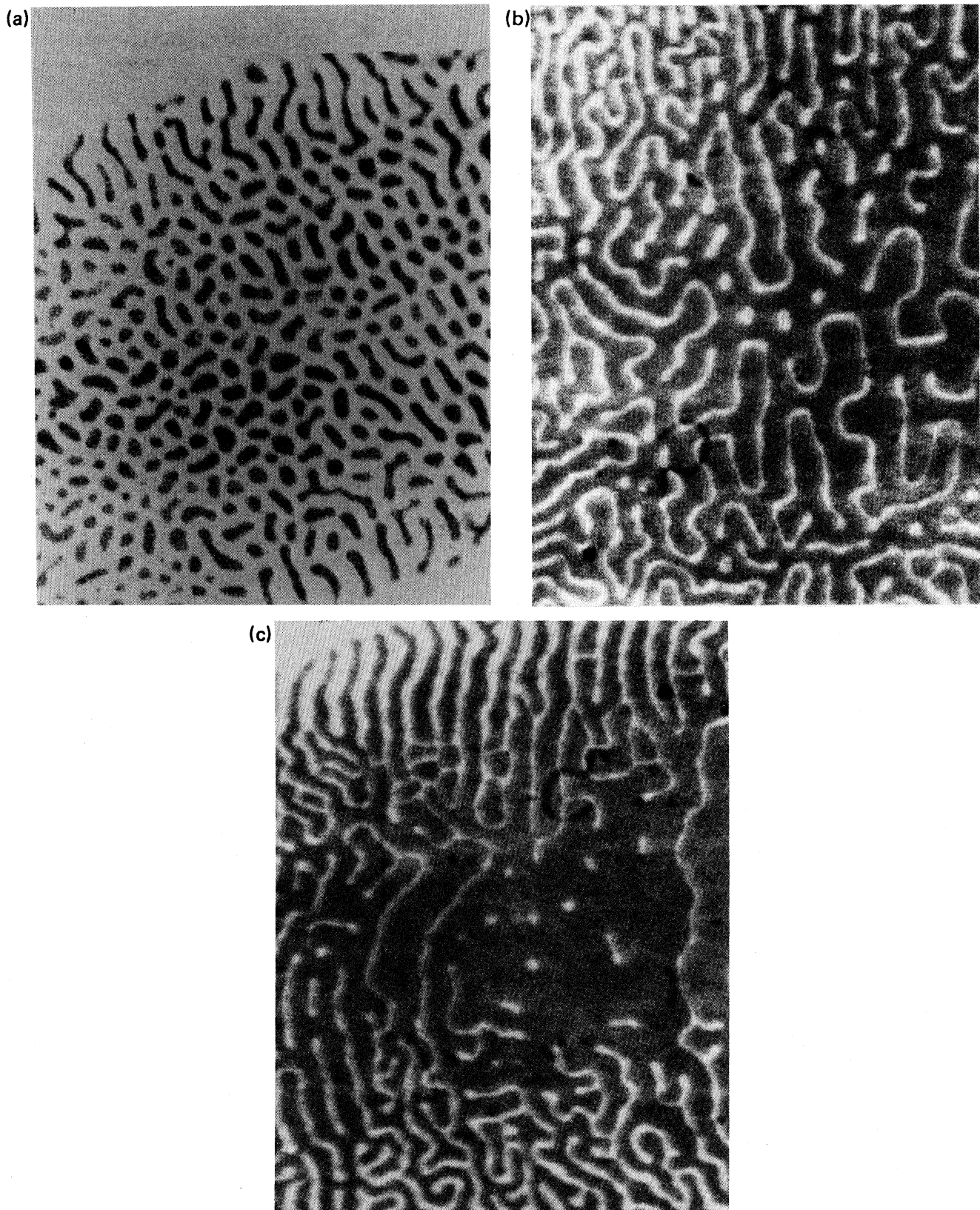

FIG. 3. A plot of the fraction of an irradiated 500-μm spot that is molten as a function of the laser intensity. The solid curve represents an average of experimental data with the plateaus corresponding successively to gratings with period λ, 2λ, etc. The other curves illustrate simple theoretical predictions for the simple grating (periodicity $= \lambda$, dashed line) and the double grating structure (periodicity $= 2\lambda$, dotted line).

FIG. 4. Photographs of disordered melt structure occurring on a 700-μm spot, corresponding to region V in Fig. 5. (a) The laser intensity is 1.7 kW cm^{-2}. The average spacing between solid regions is approximately 15 μm. (b) Illustration of the lamellae structures which form at an intensity of 2.0 kW cm^{-2}. (c) Photograph of the final disordered state existing before complete melting.

equations that corresponds to light propagating along the surface, since the Maxwell boundary conditions cannot be satisfied. However, it is expected that electromagnetic fields will still be scattered in that direction, at least in the near field. [16] These fields will be coherent with the incoming light, and the interference between the scattered and incident fields will lead to a redistribution of the optical power deposited in the sample.

Quantitative estimates of the power deposition rates as a function of position are made difficult by two considerations. The first is that the length scale associated with the melt structures is comparable to the incident wavelength so that geometrical optics is not applicable and any new theoretical model cannot be based on either expansions in λ or λ^{-1}. The second consideration is the very different optical properties of the solid and melt as Table I shows. As a result of both these features of the problem the scattered fields are expected to be very significant, and the melt structure cannot be properly considered as a uniform surface with a small perturbation.

In the previous paper[15] we offered a technique for estimating the power deposited into the locally molten (metal) and solid (dielectric) regions of the film, which overcomes the aforementioned difficulties and which accounts for the coherent redistribution of the power deposition. A convenient form for these local power deposition rates are the structural absorption coefficients η_m and η_d ($m \equiv$ metal, $d \equiv$ dielectric) defined as the (multiplicative) correction factor which would be necessary to make the geometric-optics limit agree with the true physical optics expression. The structural absorption coefficient is proportional to the power deposited per unit area relative to that deposited in a uniform layer of material.

In principle, the power deposition could be found from an exact solution of the Maxwell equations once the function $m(\mathbf{R})$ [Eq. (4.10) of Ref. 15] is specified where $m(\mathbf{R})$ is unity if the (surface) position vector $\mathbf{R}$ is within a molten region and is zero otherwise. In the approximate theory of Ref. 15, the structural absorption coefficients η_m and η_d [Eqs. (4.19) and (4.21b) of Ref. 15] are found in terms of a set of order parameters of the structure. These are the fraction f_m [$\equiv \langle m(\mathbf{R}) \rangle$] of the surface that is molten, where $\langle \ \rangle$ indicates a surface average across the laser spot, and the Fourier components of a two-point correlation function of $m(\mathbf{R})$ [Eq. (4.15) of Ref. 15]. The Appendix shows how the formalism of Ref. 15 can be applied to the calculation of power deposition in the particular, inhomogeneous structures considered here. For purposes of calculation only a truncated Fourier series of these Fourier component $c(\kappa)$ (based on the amplitude at $\kappa = 2\pi/\Lambda$ and its first four harmonics, where Λ is the fundamental spatial scale of the structure) were found to be adequate to achieve nearly full convergence in the calculation of η_m and η_d.

Several calculations of the structural absorption coefficients were performed using the constants of Table I to understood the experimentally observed relationships between the properties of the light and the induced pattern. We consider first the grating structures.

A. Ordered melt structures

For the grating structures we can take for $m(\mathbf{R})$ the function given by Eq. (B2) of Ref. 15. For the simple grating structure the period Λ equals the (lateral) thickness d_0 of the metal strips, and $\Lambda = d_0 \simeq 10.6$ μm. The absorption is then completely specified by the orientation of the linearly polarized beam relative to the grating. As in the previous paper we take ϕ to be the angle between the grating wave vector and the polarization vector, and we use $\bar{\kappa}$ to denote the principal wave number associated with the grating divided by the wave number of the incident light ($\bar{\kappa} = \lambda/\Lambda$). For example, the structure that is shown in Fig. 2(a) corresponds to $f_m \simeq 0.5$, $\phi = 0°$, and $\bar{\kappa} = 1$.

In Fig. 6 we show results in which the structural absorption coefficients of the molten and solid regions were calculated for a simple grating pattern with the experimentally observed orientation $\phi = 0°$ and the surface half molten. In the limit of geometrical optics ($\bar{\kappa} = 0$), the structural coefficient for the melt goes to unity, since the film thickness is much greater than the skin depth. However, the structural absorption coefficient for the solid *film* does not, since a completely solidified thin silicon film on sapphire would not have the reflectivity of bulk solid silicon.

In the observed structure, calculations support the idea that the power deposited in the molten regions of the grating is strongly *enhanced,* while the power deposited in the solid regions is reduced, relative to that obtained from the geometric-optics limit. In grating form the me-
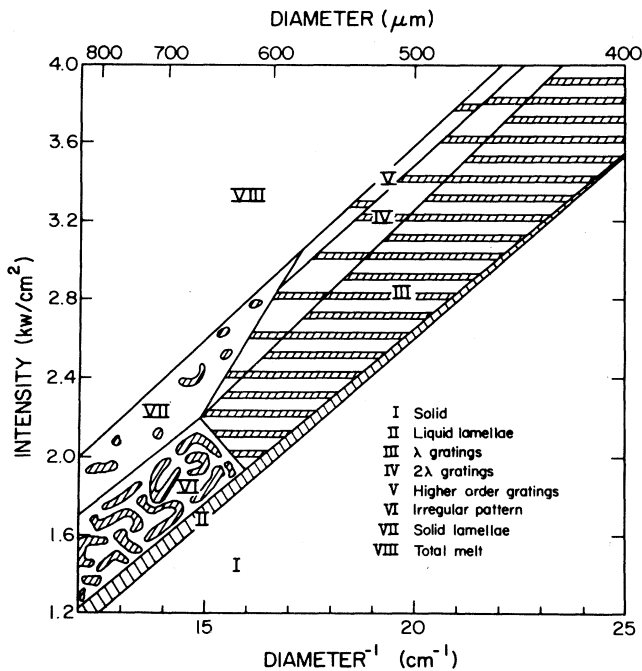
FIG. 5. The stability diagram for Si films on sapphire under laser irradiation at 10.6 μm. See text for a description of the patterns corresponding to the various regions of the diagram.
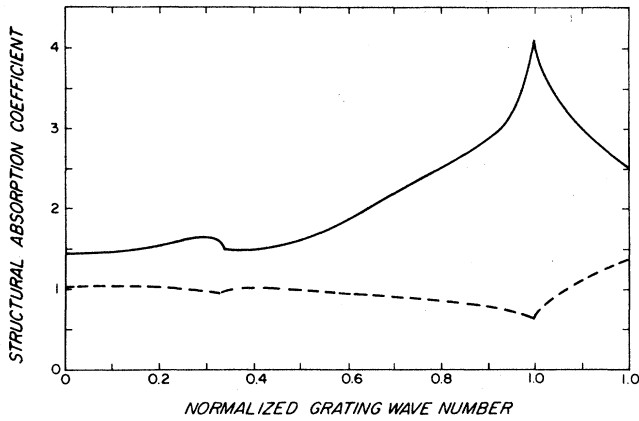
FIG. 6. The structural absorption coefficient as a function of the normalized grating wave number ($\bar{\kappa}=\lambda/\Lambda$) for a grating structure with 50% of the surface molten and with the grating wave vector parallel to the light polarization ($\phi=0°$). The broken and solid curves correspond to η_m and η_s, respectively.

tallic regions can thus sustain themselves. As was noted in the previous paper, with $f_m=0.5$ the structural absorption coefficient for the metallic region of a grating is predicted to be a maximum for $\phi=0°$, which is the experimentally observed orientation of the gratings. This point is illustrated in Fig. 7 which considers gratings similar to those above, except here with $\phi=90°$. The maximum of the energy deposition would occur in the solid in this case (which would melt, with the melt solidifying). The consistency of the theoretical and experimental results suggest that the introduction of superheated solid regions and supercooled molten regions are not required for an understanding of the melt patterns that are produced in these experiments.[17] Indeed, it appears that the melt patterns organize themselves so as to maximize the temperature of the molten regions relative to the solid regions. If scattered fields are unimportant the solid regions in the melt pattern would be hotter than the molten regions. Kurtze and Jackson[16] have shown that if the scattered fields are neglected, periodic melt patterns with a broad
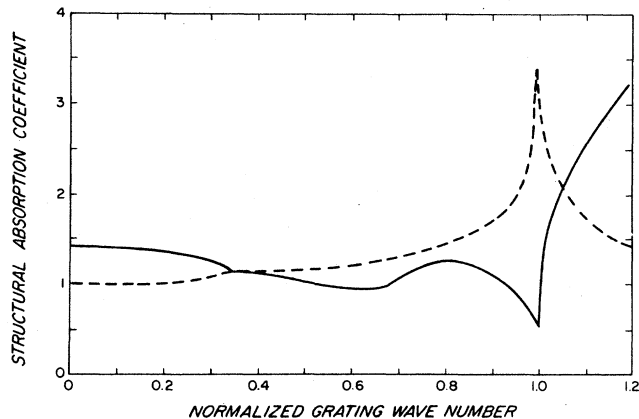
range of periodicities can still be stabilized through surface energy and heat-flow effects. Indeed it has been predicted that these effects should lead to the simple grating melt pattern having a spacing slightly larger than the incident wavelength.[18] However, this effect was not observed to within the accuracy of the experiments reported here (2%).

As Figs. 2 and 3 show, the simple grating structure remains visually unaltered over a broad range of intensities before a doubled grating structure forms with a spacing of twice the incident wavelength ($\bar{\kappa}=0.5$) and roughly 75% of the surface molten. To obtain insight into this dramatic change of periodicity, plots of η_m and η_s as a function of the normalized grating wave number were obtained. Results for a grating pattern corresponding to $f_m=0.75$ are shown in Fig. 8. A comparison with Fig. 6 reveals that the grating wave number which maximizes η_m and minimizes η_d shifts from $\bar{\kappa}=1$ to $\bar{\kappa}=\frac{1}{2}$, as f_m increases from 0.5 to 0.75. At this higher f_m, it is the harmonic term in the Fourier decomposition of the structure that is more effective in redistributing the incident energy from the dielectric to the metal. Calculations confirm that the observed orientation of the doubled grating $\phi=0°$ maximized the power deposited in the melt relative to the solid.

Similar calculations were carried out at yet larger values of f_m. At $f_m>0.8$, the criterion of maximizing the energy deposited in the melt relative to the solid leads to a prediction of gratings with spacings of three times the incident wavelength. As previously discussed, if the intensity increases, the doubled grating structures are temporarily replaced by tripled and even quadrupled gratings. However, eventually the symmetry in the direction perpendicular to the polarization was broken and the observed melt structures evolved into the lamellae array pattern. Plots of the structural absorption coefficient as a function of the fundamental grating wave number in that direction do not appear to predict a periodicity as clearly as for the other structures. However, sharp minima are indeed observed in η_s for $\bar{\kappa}=n^{-1}$, where n is an integer.

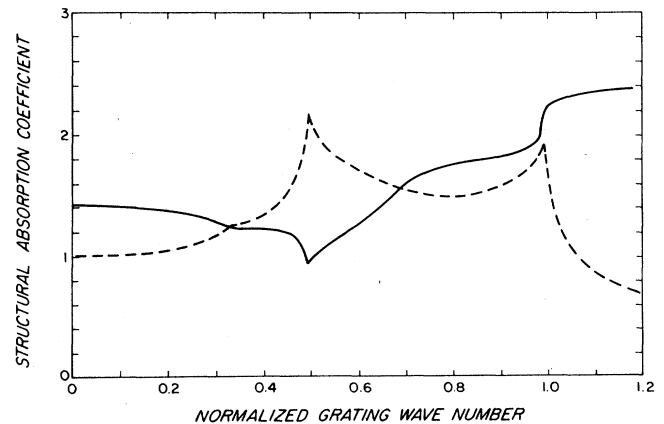

FIG. 7. Same as Fig. 6 with $\phi=90°$.

FIG. 8. The structural absorption coefficient as a function of the normalized grating wave number for a grating structure with 75% of the surface molten and with the grating wave vector parallel to the light polarization ($\phi=0°$).

In addition to gaining insight into the origin of the distinct types of ordered melt patterns, the calculations of the optical absorption of the molten and solid regions permit an estimate of the molten fraction of the surface as a function of the incident laser intensity. To model the thermal transport, a simple model was employed[19] where the back of the sapphire substrate was assumed to have a fixed uniform temperature. The heat flow was then calculated using the thermal diffusion equation and the thermal conductivities appropriate for solid and molten silicon and the sapphire substrate. A more detailed description and extension of such combined thermodynamic-electromagnetic calculations will be the subject of future publications. A comparison of the theoretical and experimental values of the fraction of the surface that melts as a function of the laser intensity is shown in Fig. 3. The assumed temperature of the back of the substrate was varied to achieve reasonable agreement with experiment, although no elaborate fitting procedure was used. In the calculation shown, the temperature at the back of the sample was set at 1200 K, which represents a reasonable estimate of the back temperature during the experiments. The theoretical plots are terminated at points corresponding to the solid regions becoming hotter than the molten regions. The calculations as carried out predict bistable behavior over a wide range of intensities. We note, however, that the calculation does not guarantee the stability of both solutions in the bistable region. Indeed, when the stability of the single and double gratings to perturbations is considered, as we do below, the bistable region vanishes. This in accordance with the lack of hysteresis in the experimentally observed transition between simple and doubled gratings.

To demonstrate the effects of perturbations on the transition between the simple and double gratings, we considered a simple model of an intermediate melt structure. This structure consists of a simple grating modified so that alternate solid regions have independent widths. Labelling the widths of the alternating solid strips as w and w', we note that as w' is reduced from w to zero, the structure evolves from the simple to a doubled grating structure. Since this structure is capable of displaying the symmetries of each of the grating structures, we refer to the pattern as a compound grating. A straightforward generalization of the treatment of Ref. 15 allows the structural absorption coefficient in each of the molten and two distinct solid regions of the compound grating to be estimated. The results of the calculation are shown in Fig. 9. The structural coefficients for the molten region and the two solid regions are plotted as a function of $(w')/\Lambda$, for $w = 0.5\Lambda$. The solid curve in the figure represents the structural absorption coefficient for the primed region and is of particular note since its slope determines the stability of the simple grating. If the slope is positive, a decrease in w' will decrease the power deposition into the primed region. As a result, even without a detailed heat-flow analysis we expect that w' will tend to increase, stabilizing the pattern. If the slope is negative, a decrease in w' will increase n_d and w' will decrease further. This would continue until n_d goes through a maximum or the primed region melts completely. A close ex-
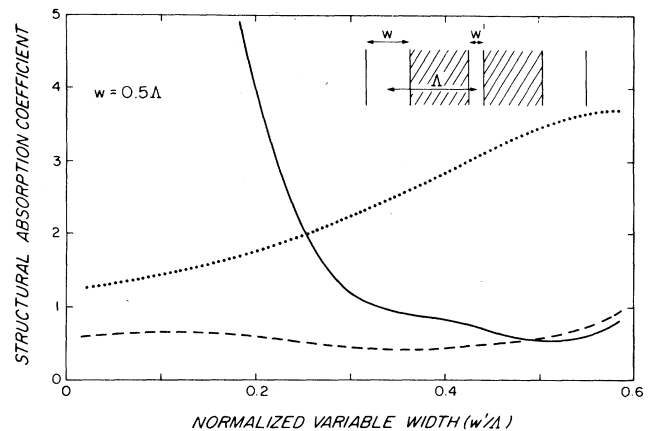

FIG. 9. Calculation of the structural absorption coefficients for the compound grating structure as a function of the width of the primed solid strips. (For explanation see text.) The dotted line corresponds to the molten strips, while the dashed and solid lines correspond to the unprimed and primed solid strips, respectively.

amination of Fig. 9 reveals a minimum of $n_{d'}$, is in the vicinity of $w'/d = 0.5$, indicating that the simple grating pattern is only marginally stable at $f_m = 0.5$. A similar analysis of the corresponding plots for $w = 0.4\lambda$ and $w = 0.6\lambda$ indicates that the simple grating pattern is clearly stable at $f_m = 0.4$, but clearly unstable at $f_m = 0.6$, with respect to the formation of a compound grating. In addition to the expectation that the simple grating structure is unstable for f_m greater than 0.5, we also expect that structures corresponding to $0 < w' < w$ should not be observed. Since the slope of $n_{d'}$ is monotonic for values of w' less than 0.5, once the pattern is unstable w' will continue to decrease until it vanishes and the doubled grating is formed. Finally we note that introducing the compound grating only permits the study of one type of instability in the simple grating. A complete understanding of the transition between the grating structures would require the consideration of a much larger set of possible instabilities in the structures, and this is beyond the scope of the present article.

B. Disordered melt structures

For experiments in which the heat-loss efficiency is low, the melt structures lack translational symmetry and long-range order. At intensities just above the melt threshold a disordered melt pattern consisting of isolated regions of molten silicon in a solid matrix was formed as shown in Fig. 4. As the intensity increases, f_m increases slowly through region VI of Fig. 5 until the silicon film makes a transition into a state corresponding to region VII. Here the size of the solid regions in the molten matrix remains relatively constant. However, f_m increases with increasing intensity as the number of solid regions per unit area decreases. For intensities just less than the threshold for complete melting, the pattern consisted of isolated solid regions interspersed in the melt. In this re-

gime, observations of the motion of the (temperature fields associated with) solid regions indicate that the solid regions do not interact, unless their spacing becomes comparable to the wavelength of the incident light. Further, during "collisions" in which the solid regions are apparently interacting, the regions do not come into contact and maintain their identity. It appeared that the isolated solid regions behave like actual "particles" rather then excursions in the temperature field of the film. At intensities just above the initial melt threshold, isolated molten regions behaved similarly, prior to forming a steady-state melt pattern. The most notable distinction between the dynamics of the isolated molten and solid regions is that the molten regions occasionally do come into contact and fuse together during their collisions. The size of this region subsequently reduces to the size of one of the original molten regions. Thus, it is possible for the molten regions to coalesce during collisions.

The observations reported in the preceding paragraph indicate that some insight into the disordered melt patterns can be obtained through an approach wherein individual molten or solid regions are first studied in isolation, with the interactions between regions introduced subsequently. As a first step, let us consider a single isolated region of molten silicon. Although in the observed melt pattern the molten regions could be quite irregular in shape, we assume a disc geometry for simplicity. The structural absorption coefficient of an isolated molten disc as a function of radius is shown in Fig. 10. This calculation was in fact made assuming a periodic array of such discs so that the formalism of Ref. 15 could be applied. But the results were found to be essentially independent of the period of the array, as long as it was considerably larger than the disc size and the wavelength of light. Care was also taken to avoid periodicities which were multiples of the incident wavelength. The results of this calculation indicate that the power deposition drops rapidly with increasing radius in the vicinity of 3 μm, and then slowly approaches the geometrical optics limit. Under the assumption that the disc loses thermal energy at a rate proportional to the area of the melt-sapphire interface, we can calculate the disc radius as a function of
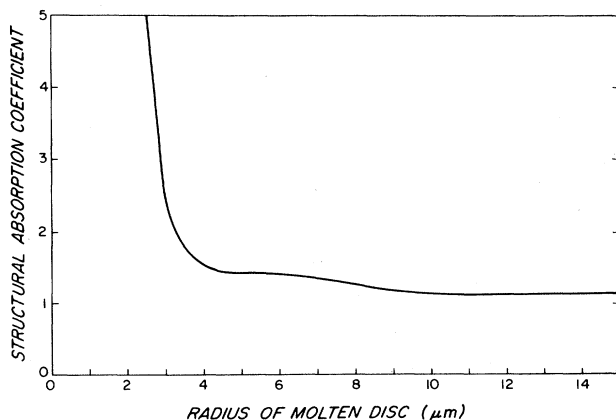
laser intensity. Results of the calculation indicate that as the intensity increases from disc formation threshold, the size of the disc rapidly increases to a value of $\simeq 3$ μm, and this radius increases by less than 30% as the intensity further increases by a factor of 5. This result is in good agreement with Fig. 4(a), even though only an isolated disc has been chosen for the calculation and surface tension effects have been ignored.

Next, the interaction between two such discs can be considered taking the light to be polarized along the axis of separation. In Fig. 11, a plot of the structural absorption coefficient for each of two disc-shaped molten regions is given as a function of their separation. As discussed in the Appendix, the calculation was made by actually assuming a periodic array of pairs of discs, with the period of the array much larger than both the disc size and the distance between the pairs. The slope of the graph can be used as the basis of a plausibility argument, similar to that given for the compound grating above, and based on the empirical criterion that the most stable structures maximize energy deposition in the melt relative to the solid (Sec. IV A). It is clear that the power absorbed by the molten regions is maximized for separations of approximately 16 μm. Fluctuations which would try to increase or decrease this separation would reduce the power absorbed by the discs making their formation less likely. The calculated optimum spacing corresponds closely to the average spacing between the molten regions of approximately 15 μm, in the type of melt pattern shown in Fig. 4(a). The sizes and distance quoted here will change slightly for the orthogonal polarization state.

The results of calculations carried out assuming isolated discs of solid silicon are similar to those discussed above although some of the implications are quite different. In Fig. 12 the plot of the structural absorption coefficient as a function of disc radius shows a dramatic enhancement as the radius is reduced below approximately 3 μm. Solid discs of less than this size are therefore unstable since the negative slope of the average power deposition destabilizes the solid region with respect to its size. The plot of Fig. 12 predicts a minimum radius,

FIG. 10. The structural absorption coefficient of a disc of molten silicon as a function of its radius.
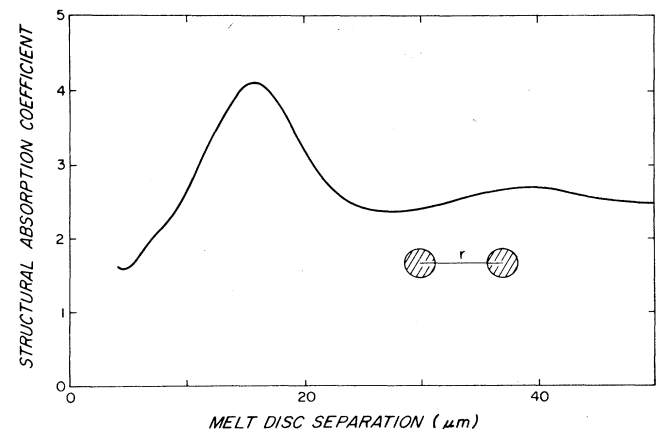

FIG. 11. The structural absorption coefficient of two discs of molten silicon as a function of their separation. The radii of the discs were assumed to be 3.0 μm.
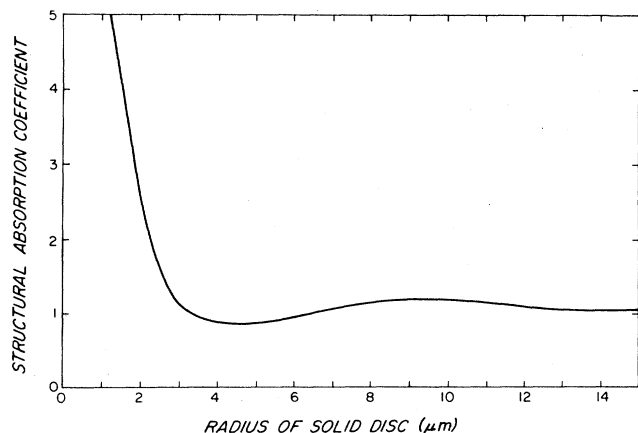
FIG. 12. The structural absorption coefficient of a disc of solid silicon as a function of its radius.

above which isolated solid regions can be stable corresponding to that portion of the plot with positive slope. This agrees with the experimental observation that the solid regions disappeared sharply as the laser intensity was increased. The minimum size for stable solid regions is on the order of 6 μm from Fig. 12 which corresponds quite well to the experimentally determined radii of the solid discs at intensities just below the threshold for complete melting. In Fig. 13 we display the structural absorption coefficient for two solid discs as a function of their separation. The polarization of the light field is taken as parallel to the line joining the centers of the discs. Minimizing the power deposited into the solid would lead to a predicted separation of 16 μm. (Slightly higher separations were calculated for other polarization states of the light.)

The calculations of the structural absorption coefficients for the molten and solid discs, both in isolation and during their interaction, allow the collisional behavior to be understood in more detail. The size of the molten or solid region is determined primarily by the
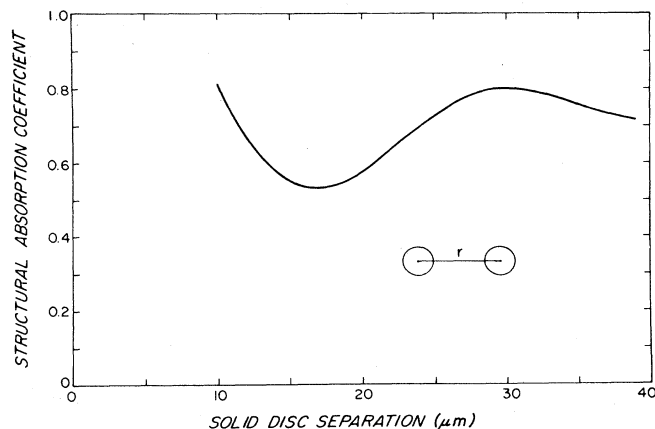

FIG. 13. The structural absorption coefficient of two discs of solid silicon as a function of their separation. The radius of the discs were assumed to be 5.0 μm.

modification to the energy absorption rate that can be attributed to its own structure. Separations between adjacent molten or solid regions are determined by the influence of fields scattered from one region to its neighbors. Depending on the separation between the regions, the scattered fields will add either constructively or destructively with the incident light and hence increase or decrease the absorption in the region. In both cases, the modification of the energy absorption rates due to the presence of a second region destabilizes the structures at small separations, increasing the power absorbed by a solid disc and decreasing the power absorbed by a molten disc. The molten regions are capable of compensating the decrease in the absorbed power due to the interaction by reducing their size. The sizes of the solid regions already approximately correspond to the minimum in the power absorption, and hence the increase in the absorbed power due to the interaction cannot be compensated. As a result, the configuration of the solid regions close to each other cannot be stabilized, and we cn understand why this structure is not observed.

While the approach taken above provides considerable insight into all of the disordered melt structures, the direct comparison of the calculations to the experimental results is limited to the disordered melt patterns observed just above the initial melting threshold, region II in the phase diagram, and to the region just below the threshold for complete melting, the upper portion of solid regions are elongated structures with a well-defined width. Approximately their shapes as discs are unjustified. Further, the solid regions are closely spaced under the conditions corresponding to region VII, so that three-body interactions are probably important in their detailed theoretical treatment. However, some selected features of the disordered structures in these regions can be compared with the calculations. The width of the elongated solid structures is only about 1 μm less than the predicted disc diameter, and the average perpendicular spacing between the solid regions is reasonably close to the predicted disc separation. Furthermore, a close inspection of any of the photographs, corresponding to regions VI or VII, reveals that each end of a solid region terminates at a disclike protrusion, with a diameter slightly larger than the cross section of the elongated portion. The agreement between this experimental disc size and the disc size predicted from Fig. 12 is quite good.

V. SUMMARY

To summarize, we have studied the melt structures associated with cw laser-induced melting of silicon films. The experimental parameters which were found to control the pattern formation processes were the incident laser intensity, the spot size of the laser beam, and the amount of lateral heat flow within the silicon film. Although all of our experiments were conducted at normal incidence and with a linearly polarized beam, we identified a large number of distinct types of structures, in direct contrast to the melt patterns developed during pulsed laser melting. We emphasize the role of the coherent power deposition, since it initially generates the

instabilities that eventually lead to the melt structures. However, although the inhomogeneous energy deposition is responsible for the initial symmetry breaking, once melting has been initiated the heat flow is an equal partner in determining the steady-state pattern. In cases where the spot size is relatively small (and hence a higher laser intensity is required to initiate melting), the coherent energy deposition appears to dominate, and simple geometric patterns result. For larger spot sizes, the patterns are irregular with the coherent deposition of energy imposing constraints on the sizes and separation of adjacent regions, but not determining the overall pattern formation. The relative roles in the formation of the irregular patterns of the initial conditions, material properties, thermal transport, and the coherent energy deposition is the subject of an ongoing study.

In cases where the coherent power deposition determines the patterns, we carried out systematic observations to uncover new types of melt patterns and clarify the relationship between the different states. These were summarized in the stability diagram of Fig. 5. Calculations of the optical absorption in the solid and molten regions enabled us to understand the symmetry of the ordered states, calculate the fraction of the surface molten as a function of incident intensity, and gain insight into key features of the disorder patterns and their dynamics. The general criterion which we found could be used to understand the relative stability of different structures

was that the more stable structures maximize the energy deposition in the melt relative to the solid. Although not unreasonable, this criterion requires a fundamental justification which at this time we cannot supply, This, and the observation and elucidation of similar optically-induced structures in other materials undergoing phase transitions are subjects for future study.

ACKNOWLEDGMENTS

APPENDIX

In this Appendix, a simple technique will be developed for applying the formalism of Ref. 15 (previous paper) to estimate the optical absorption in the melt structures. This is facilitated by a simple relation between the two-point correlation function $c(\Delta R)$ and the Fourier transform of the label function $m(R)$. We will begin by invoking the Wiener-Khinchin theorem in two dimensions which simply relates the Fourier transform of an autocorrelation function to the square of the amplitudes of the Fourier components of the original function. Using the same convention for the Fourier transform as Ref. 15 we have

$$\int_{\Delta R} d\Delta R \exp(-i\kappa \cdot \Delta R) \int_R dR \, m(R)m(R-\Delta R) = \int_{\Delta R} d\Delta R \int_R dR \exp[i\kappa \cdot (R-\Delta R)]\exp(-i\kappa \cdot R)m(R)m(R-\Delta R)$$
$$= m(\kappa)m(-\kappa) = m(\kappa)m^*(\kappa) ,$$

where we have used R and ΔR are independent so that the integration variables can be changed to R and $R-\Delta R$. The two-point correlation function defined in Ref. 15 [Eq. (4.15)] can be simply related to the autocorrelation function so that

$$c(\kappa) = \frac{1}{f_m f_d} m(\kappa)m^*(\kappa) - \frac{f_m}{f_d}\delta(\kappa) ,$$

where here we identify the ensemble average introduced in Ref. 15 with a suitable average over the surface. If we assume that the label function m is periodic, then we can decompose it into an appropriate Fourier series, and it is straightforward to describe the two-point correlation function in terms of the Fourier coefficients. We then have

$$m(R) = \sum_{n,m=0}^{\infty} [a_{nm}\cos(\kappa_n x)\cos(\kappa_m y)$$
$$+ b_{nm}\cos(\kappa_n x)\sin(\kappa_m y)$$
$$+ c_{nm}\sin(\kappa_n x)\cos(\kappa_m y)$$
$$+ d_{nm}\sin(\kappa_n x)\sin(\kappa_m y)]$$

with

$$a_{nm} = 4\frac{\Lambda_{nm}}{L_x L_y}\int_{-L_x/2}^{L_x/2}\int_{-L_y/2}^{L_y/2}dx\,dy\,m(R)\cos(\kappa_n x)$$
$$\times \cos(\kappa_m y) ,$$

$$b_{nm} = 4\frac{\Lambda_{nm}}{L_x L_y}\int_{-L_x/2}^{L_x/2}\int_{-L_y/2}^{L_y/2}dx\,dy\,m(R)\cos(\kappa_n x)$$
$$\times \sin(\kappa_m y) ,$$

$$c_{nm} = 4\frac{\Lambda_{nm}}{L_x L_y}\int_{-L_x/2}^{L_x/2}\int_{-L_y/2}^{L_y/2}dx\,dy\,m(R)\sin(\kappa_n x)$$
$$\times \cos(\kappa_m y) ,$$

$$d_{nm} = 4\frac{\Lambda_{nm}}{L_x L_y}\int_{-L_x/2}^{L_x/2}\int_{-L_y/2}^{L_y/2}dx\,dy\,m(R)\sin(\kappa_n x)$$
$$\times \sin(\kappa_m y) ,$$

where $\Lambda_{00} = \frac{1}{4}$, $\Lambda_{n0} = \Lambda_{0m} = \frac{1}{2}$, $\Lambda_{nm} = 1$ for $n,m \neq 0$ and L_x, L_y are the periods in the $\hat{x}$ and $\hat{y}$ directions.

Substituting for $m(R)$ in the expression for $c(\Delta R)$ yields

$$c(\Delta\mathbf{R}) = \frac{1}{f_m f_d L_x L_y} \int_{-L_x/2}^{L_x/2} dx \int_{-L_y/2}^{L_y/2} dy \sum_{n,m=0}^{\infty} \sum_{n',m'=0}^{\infty} [a_{nm}\cos(\kappa_n x)\cos(\kappa_n y) + \cdots]$$

$$\times \{a_{n'm'}\cos[\kappa_{n'}(x+\Delta x)]\cos[\kappa_{n'}(y+\Delta y)] + \cdots \} - \frac{f_m}{f_d} .$$

The order of the summations and the integrations can be reversed and the required integrations can then be carried out. After collecting similar terms we have

$$c(\Delta\mathbf{R}) = -\frac{f_m}{f_d} + \frac{1}{4 f_m f_d} \left[\sum_{n,m} \{a_{nm}^2(1+\delta_{n0})(1+\delta_{0m}) + b_{nm}^2(1+\delta_{n0}) + c_{nm}^2(1+\delta_{0m}) + d_{nm}^2 \}\cos(\kappa_n \Delta x)\cos(\kappa_m \Delta y) \right.$$

$$\left. + \sum_{n,m} 2(a_{nm}d_{nm} - b_{nm}c_{nm})\sin(\kappa_n \Delta x)\sin(\kappa_m \Delta y) \right] .$$

Note that $c(\Delta\mathbf{R}) = c(-\Delta\mathbf{R})$ as expected.

The above allows the optical absorption by a melt structure to be estimated given the Fourier components present in the structure. The results presented in this paper were obtained by describing the melt structure in terms of a truncated Fourier series. The absorption by nonperiodic structures were estimated by calculating the absorption in an equivalent periodic structure produced by replicating the nonperiodic structure on a length scale much greater than the wavelength or size of the structure. For example, the absorption of an isolated solid disc was estimated by calculating the absorption in an array of solid discs separated by a distance L much greater than the incident wavelength or the disc radius. In such cases, the absorption was calculated for several values of L to ensure that the calculated absorption was not an artifact of the artificial periodicity.

*Present address: Department of Physics, University of Illinois at Urbana-Champaign, 1110 West Green Street, Urbana, IL 61801, and Materials Research Laboratory, University of Illinois at Urbana-Champaign, 104 South Goodwin Avenue, Urbana, IL 61801.

[1] See, for example, *Energy Beam-Solid Interactions and Transient Thermal Processing, Proceedings of the Materials Research Society,* edited by D. K. Biegelsen, G. A. Rozgonyi, and C. V. Shank (Materials Research Society, Pittsburgh, 1985).

[2] J. F. Young, J. E. Sipe, M. I. Gallant, J. S. Preston, and H. M. van Driel, in *Laser and Electron Beam Interactions with Solids,* edited by B. R. Appelton and G. K. Celler (North-Holland, Amsterdam, 1982), p. 233; J. F. Young, J. S. Preston, J. E. Sipe, and H. M. van Driel, Phys. Rev. B **27**, 1424 (1983); J. F. Young, J. E. Sipe, and H. M. van Driel, *ibid.* **30**, 2001 (1984).

[3] S. A. Akhmanov, V. I. Emel'yanov, N. I. Koroteev, and V. N. Seminogov, Usp. Fiz. Nauk **147**, 675 (1985) [Sov. Phys.—Usp. **28**, 1984 (1985)].

[4] A. E. Siegman and P. M. Fauchet, IEEE J. Quantum Electron **QE-22**, 1384 (1986).

[5] S.R. Brueck and D. J. Ehrlich, Phys. Rev. Lett. **48**, 1678 (1982).

[6] M. J. Soileau, IEEE J. Quantum Electron **QE-20**, 464 (1984).

[7] A. M. Prokhorov, V. A. Sychugov, A. V. Tishchenko, and A. A. Khakimov, Pis'ma Zh. Tekh. Fiz. **9**, 65 (1983) [Sov. Phys.

Tech. Lett. **9**, 28 (1983)].

[8] I. Ursu, I. N. Mihailescu, Al. Popa, A. M. Prokhorov, V. I. Konov, V. P. Ageev, and V. N. Tokarev, Appl. Phys. Lett. **45**, 365 (1984).

[9] M. A. Bosch and R. A. Lemons, Phys. Rev. Lett. **47**, 1151 (1981).

[10] D. K. Biegelson, R. J. Nemanich, L. E. Fennel, and R. A. Street, in Ref. 1, p. 383.

[11] W. G. Hawkins and D. K. Biegelson, Appl. Phys. Lett. **42**, 358 (1983).

[12] J. S. Preston, H. M. van Driel, and J. E. Sipe, Phys. Rev. Lett. **58**, 69 (1987).

[13] H. M. van Driel, J. E. Sipe, and J. F. Young, Phys. Rev. Lett. **49**, 1955 (1982).

[14] *Pattern Recognition in Physical, Chemical, and Biological Systems,* edited by H. Haken (Springer-Verlag, New York, 1980).

[15] J. S. Preston, J. E. Sipe, H. M. van Driel, and J. Luscombe, Phys. Rev. B **40**, 3931 (1989).

[16] J. S. Preston, H. M. van Driel, and J. F. Young, Can. J. Phys. **63**, 104 (1985); J. E. Sipe, J. F. Young, J. S. Preston, and H. M. van Driel, Phys. Rev. B **26**, 1411 (1983).

[17] K. A. Jackson and Douglas A. Kurtze, J. Cryst. Growth **71**, 385 (1985).

[18] Douglas A. Kurtze and Chuanjing Ji, Phys. Rev. Lett. **59**, 1060 (1987).
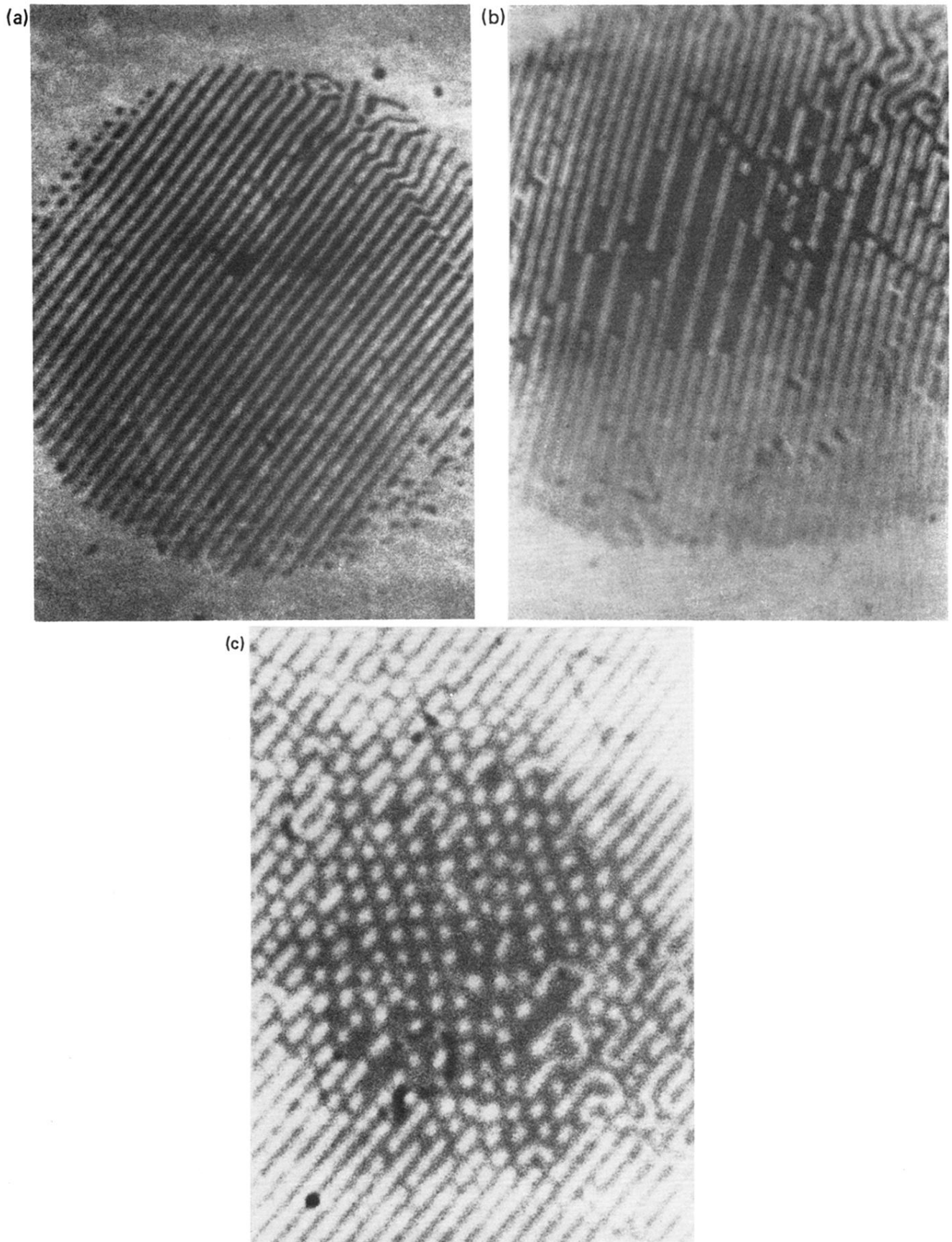
[19] J. S. Preston, Ph.D. thesis, University of Toronto, 1987.

FIG. 2. Photographs of laser-generated melt patterns which exhibit long-range order for a spot size of 500 μm: (a) that of a simple grating of period 10.5±0.1 μm occurring for a laser intensity of 2.7 kW cm^{-2} corresponding to region III in Fig. 5; (b) photograph of the interior portion of a spot illuminated at 3.2 kW cm^{-2}; the simple grating has been replaced by the doubled grating structure; (c) in the central portion of the photograph, the solid regions are aligned in the lamellae array pattern. The laser intensity is 3.4 kW cm^{-2}.
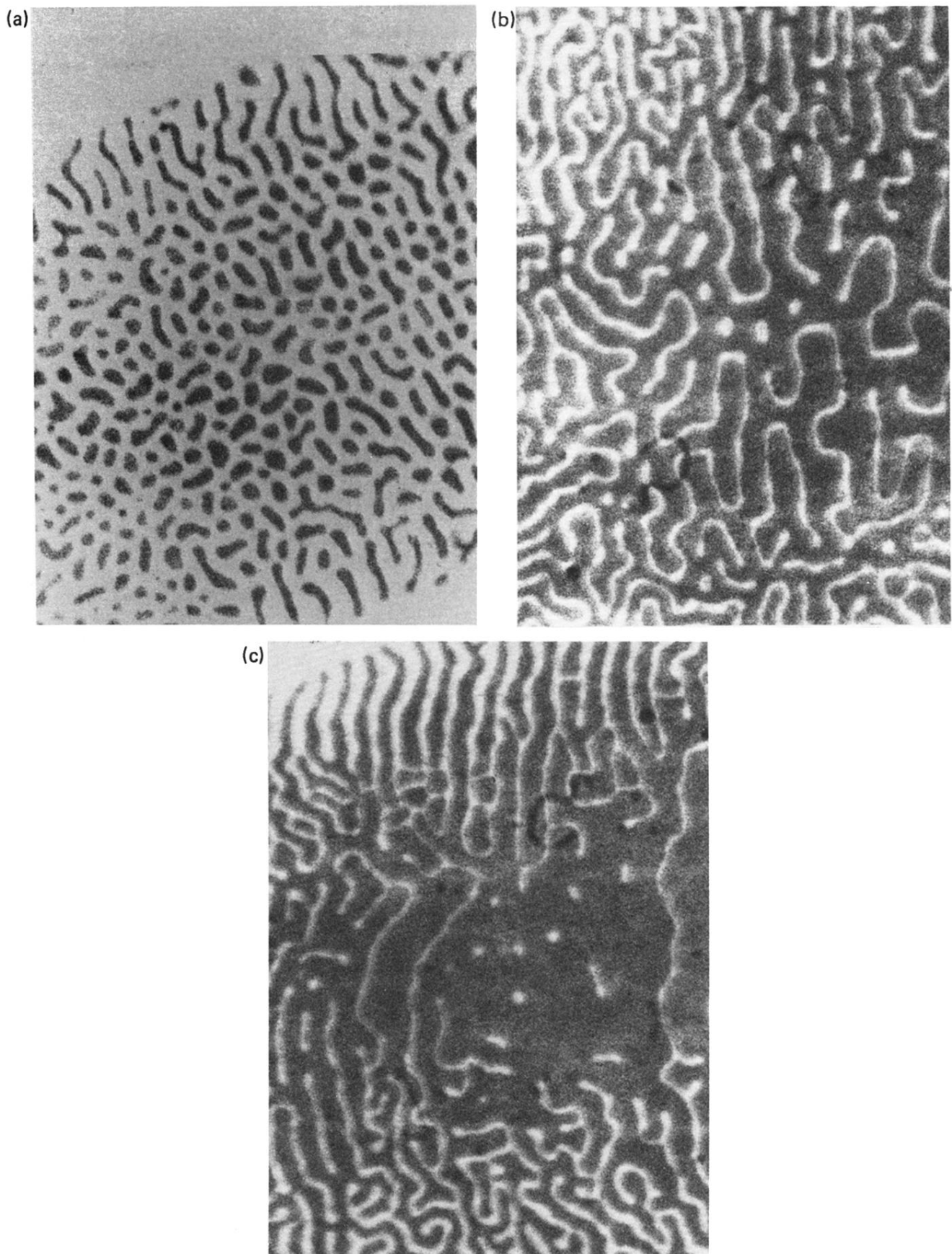
FIG. 4. Photographs of disordered melt structure occurring on a 700-μm spot, corresponding to region V in Fig. 5. (a) The laser intensity is 1.7 kW cm^{-2}. The average spacing between solid regions is approximately 15 μm. (b) Illustration of the lamellae structures which form at an intensity of 2.0 kW cm^{-2}. (c) Photograph of the final disordered state existing before complete melting.